Proceedings of the ICBBG2025
2025 International conference on Bio-mediated and Bio-inspired Geotechnics
18-20 May, 2025 | Tempe, Arizona, USA
https://doi.org/10.53243/ICBBG2025-83

Discrete Element Modeling Simulations of Interfaces Between Snakeskin-Inspired Surfaces and Sand

D. Nguyen, M.S.[1], and A. Martinez Ph.D.[2]

[1]University of California Davis, Department of Civil & Environmental Engineering, 2001 Ghausi Hall, Davis, CA, USA; E-mail: dtlnguyen@ucdavis.edu
[2]University of California Davis, Department of Civil & Environmental Engineering, 2001 Ghausi Hall, Davis, CA, USA; E-mail: amart@ucdavis.edu

ABSTRACT

Soil-structure interface friction is a crucial feature of many geotechnical systems. These systems may benefit from directionally dependent skin friction, where greater strength is developed in a particular direction. To this end, inspiration is taken from snakes' ventral scales, which enable easy forward sliding with increased friction in the reverse direction. Previous experimental investigations have shown that snakeskin inspired surfaces can mobilize larger skin friction magnitude when sheared against the asperities (i.e. cranially) than along the asperities (i.e. caudally). The behavior of these interfaces is explored using discrete element modelling (DEM). Interface shear simulations are performed on sand specimens in contact with snakeskin-inspired surfaces with varying asperity height and length as well as with reference smooth and rough surfaces. The simulations shed light on the influence of the asperity geometry on the shear behavior. Analysis of the evolution of particle displacements and contact networks augment the understanding of load transfer processes. During cranial shearing, significant bearing forces mobilized on the backsides of asperities contribute to greater strengths and mobilize individual failure surfaces. In contrast, slippage between the asperities and the particles is the primary failure mode during caudal shearing. These insights can provide additional guidance for efficient design of snakeskin-inspired surfaces for engineering applications.

INTRODUCTION

Geotechnical infrastructure is typically designed to mobilize similar friction angles in any direction. However, a wide variety of applications may benefit from directionally dependent shear strength. For example, deep foundation systems and soil anchors can benefit from having greater pullout capacities while maintaining low installation forces. To this end, inspiration is taken from the ventral scales on the underbelly of snakes. The shape of these scales allows snakes to slide forward easily while having increased interface friction in the reverse direction, allowing them to anchor the bodies to the ground. Geotechnical technologies can adopt similar geometries to these scales, creating directionally dependent soil-structure interfaces.

Investigations of soil-structure interface shear have revealed that the behavior is influenced by the roughness of the structural material (Uesugi and Kishida 1986), loading conditions (Martinez and Frost 2018), and soil properties (DeJong and Westgate 2009; Dietz and Lings 2006). The effect of the latter is similar to that observed in soil tests, with strength and dilatancy increasing with increased particle angularity and soil density. Sufficiently rough surfaces lead to failure of the sand mass, whereas sufficiently smooth surfaces lead to sliding at the points of contact with the particles. By increasing the roughness of randomly textured surfaces, the interface strength increases up to a maximum value equal to the soil's angle of internal friction (Dietz and Lings 2006). However, the internal soil frictional angle can be exceeded by the interface strength when there is sufficient spacing between asperities making up the shear surface (Hryciw and Irsyam 1993; Martinez and Frost 2017). The shape of these asperities influences interface shear response (Frost and DeJong 2005; Martinez and Frost 2017).

Investigations have been conducted on the interface shear behavior of snakeskin-inspired surfaces. Experiments have shown that the shear behavior depends on both the shear direction and geometry of the asperities. Larger shear resistances and deformations develop during cranial shear. In this shear direction, asperities with smaller lengths (L) and greater heights (H) mobilize greater resistances and induce uniform deformation patterns. In contrast, asperities with smaller H or greater L produce localized wedgelike zones with intense deformation ahead of asperities. Significantly less resistance and deformations occur during caudal shear, whose behavior is influenced by the asperity slope (Martinez et al. 2019). Several studies such as Lee et al. (2023) used interface direct shear tests and reported similar behaviors, showing the greater shear resistances and more dilative behavior of interfaces sheared in the cranial directions in comparison to the caudal one. The degree of particle breakage has been found to be much higher and more sensitive to normal stress during cranial shear, and the amount of particle breakage increased with increasing H and decreasing L (Xiao et al. 2023). The shear mechanisms of different snakeskin-inspired patterns have also been linked to the number of particles in contact with asperities, with an increase in contacts resulting in increases in the shear resistances regardless of shear direction (Gayathri et al. 2022). Greater strength in the cranial direction than in the caudal one have also been reported from investigations on the monotonic and cyclic response of snakeskin-inspired piles tested in the centrifuge (O'Hara and Martinez 2021 and 2024) and in DEM simulations (Zhong et al. 2021). These studies have also found that the peak and residual shear resistance have a well-defined relationship with the ratio of asperity length to height (L/H). Specifically, as L/H increases, shear resistance decreases while exhibiting a diminishing rate of reduction as L/H grows.

The particle-scale interactions present at soil-structure interfaces can be further investigated with DEM simulations to obtain particle-level information. The evolution of particle displacements, rotations, and contact forces can be examined, revealing the micro mechanisms governing the globally-observed behaviors. DEM simulations can also avoid the boundary effects present in experimental investigations that may influence the measured response, such as box friction. As such, these investigations can both reaffirm past studies and uncover new mechanisms.

SIMULATION SET-UP

Monotonic interface shear simulations were performed on PFC 3D version 5.0 (Itasca, Minneapolis, MN) using a linear contact model with rolling resistance. Contacts are represented by spring and dashpot components. Springs with normal and shear stiffnesses (k_N and k_S) provide linear elastic frictional behavior. k_N is equal to the product of the particle diameter (d) and elastic stiffness modulus (E) and k_S is calculated based on a stiffness ratio (k_N/k_S). Dashpots of normal and shear damping ratios (β_N and β_S, respectively) provide viscous damping. A coulomb limit on shear force, defined by μ, models interparticle friction. Additionally, rolling resistance is added by limiting relative rotation to a maximum value defined by μ_r.

For this study, the contact parameters of the simulated material are calibrated to match the behavior of Ottawa F65 sand. Ottawa F65 sand is a poorly-graded, sub-rounded sand with a median particle size (D_{50}) of 0.21 mm, coefficient of uniformity (C_U) of 1.64, and coefficient of curvature (C_C) of 1.01. All specimens were compacted to the same initial relative density (D_r) before shearing. D_r was controlled by adjusting the initial values of μ and μ_r during compaction. Low values of μ and μ_r enable tight packing while high μ and μ_r values prevent void spaces from collapsing during compaction. In order to obtain a dilative specimen, a high initial D_r of 84% was selected, which was created with $\mu_0 = 0.06$ and $\mu_{r0} = 0.2$. After the compaction process and before shearing commences, μ and μ_r are then set to calibrated values that produces shear behavior closest to Ottawa F65 sand shown in Table 1. Calibration was achieved through triaxial test simulations, where contact parameters were adjusted until matching behaviors were established between DEM simulations and experimental datasets from Blair (2024). Table 1 lists the DEM parameters obtained from this calibration procedure, while Figure 1a compares the stress-strain behavior of triaxial test simulations and experiments. Figure 1b shows the grain size distribution (GSD) of Ottawa F65 sand and the simulated sand used in these investigations. During calibration, an unscaled GSD was used. For interface shear simulations, the GSD was upscaled by a factor of 20 to reduce computational times.

Table 1. Particle parameters for simulated Ottawa F65 sand.

Parameter	*Value*
Interparticle friction, μ	0.51
Rolling resistance, μ_r	0.26
Wall friction, μ_k	0.20
Stiffness modulus, E (Pa)	1.00E+08
Stiffness ratio, k_N/k_S	1.50
Damping ratios, β_N and β_S	0.10
Density, ρ	2650

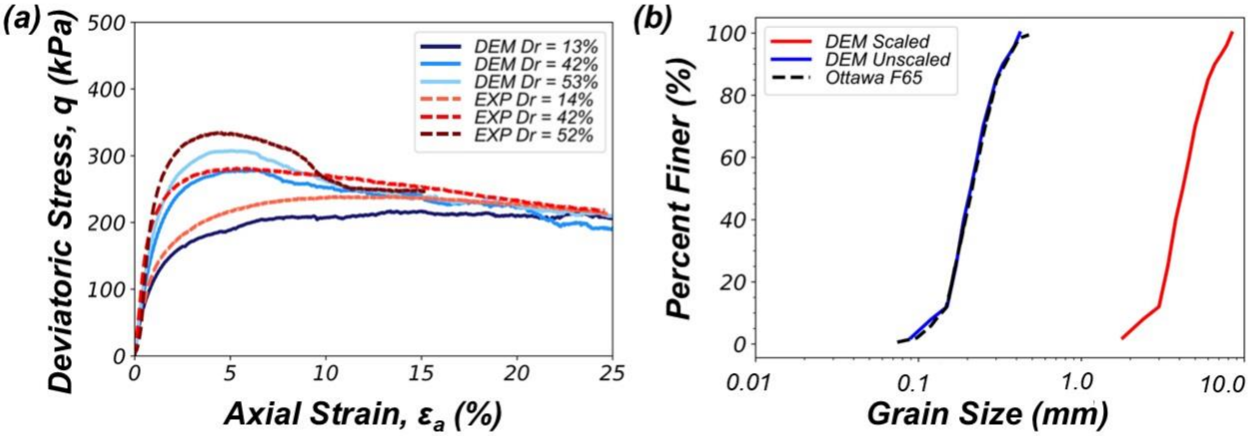

Figure 1. Comparison of triaxial stress-strain behavior between calibrated DEM simulations and experimental results for Ottawa F65 sand (a). GSDs of scaled DEM sand (for interface shear), unscaled DEM sand (for calibration), and Ottawa F65 sand (b).

The simulations were performed on rectangular shear boxes, as shown in Figure 2a. The top and bottom of the specimen are bounded by rigid walls. The top of the specimen consists of a series of lateral, evenly spaced plates which displace independently from one another to maintain a constant normal stress (σ_N). Vertical hamper walls are placed in between these plates to create a layer of fixed particles near the top of the specimen during shear and to keep particles from leaking out of the shear box as the top plates displace. The interval of the hamper walls was reduced until the influence of hamper wall spacing on shear behavior was insignificant. The depths of hamper walls are chosen so that they are just deep enough to keep a layer of particles fixed to the top surface after σ_N is applied to the top plates. The shear surface at the bottom of the specimen, whose geometry can be changed depending on the surface being modeled, is displaced horizontally during the shearing phase. For snakeskin-inspired surfaces, the direction in which the particles move against scales is referred to as the cranial direction. The opposite direction in which particles move over the smooth surface of the scales is the caudal direction. These directions are illustrated in Figure 2b. The front, back, left, and right sides of the specimen are bounded by periodic boundaries, allowing the simulation to model an infinitely large plane of granular material. The size of the specimen was chosen after a size sensitivity study, as discussed below. To reduce computational costs, the dimensions of all objects, including both particles and rigid walls, were upscaled by a factor of 20.

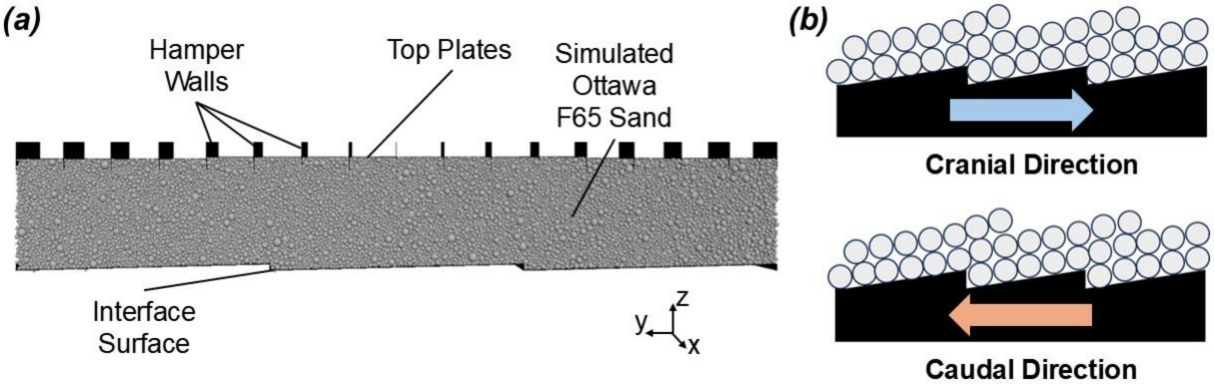

Figure 2. Specimen for simulations (a), cranial and caudal directions (b).

Interface shear simulations are performed on five different surfaces with varying geometries. The smooth reference surface consists of a flat surface with no asperities. The rough reference surface is constructed with a sawtooth pattern similar to the surfaces used by Jensen et al. (1999) and Jing et al. (2018) with a tooth length equivalent to 2.5 D_{50}. The three snakeskin inspired surfaces consist of straight-lined, right-triangular scale shapes inspired after the scales of a western hognose snake (Martinez et al. 2019). These surfaces had asperity heights (H) and lengths (L) normalized by D_{50} of 1.4 and 29, 1.4 and 57, and 0.5 and 29. The naming convention of the snakeskin inspired surfaces is H#L&-XX, where # is the asperity height/D_{50}, & is the asperity length/D_{50}, and XX is 'CR' or 'CD' which indicates the cranial or caudal directions respectively. Three snakeskin-inspired surfaces are used, including H1.4L29, H1.4L57, and H0.5L29.

The simulations consist of three phases: specimen preparation, compression, and shearing. During specimen preparation, an initial state is created where particles are placed randomly in the shear box, forming a non-contacting cloud of spheres. Upon filling the box, the system is cycled to resolve the overlaps and calm particles. Then, a normal effective stress (σ'_N) of 80 kPa is applied by the top plates and is maintained through servo control. Shearing then commences by displacing the bottom surface quasi-statically until a horizontal displacement equivalent to 28.6 D_{50} (i.e. 120 mm) is accrued. Gravity is not modeled during these simulations.

Before the main investigation, a specimen size sensitivity study was conducted to determine the dimensions needed to eliminate boundary effects. The width, height, and length of the shear box were incrementally increased until further changes did not affect the interface behavior. The shear behavior had little sensitivity to the box width; thus, a width equivalent to 14 D_{50} was chosen. The length of the specimen dictates how many asperities are present in the specimen. A length equivalent to 171 D_{50} was chosen to avoid creating partial asperities for the tested surface geometries. The geometry of the shear surface influenced the sensitivity of the shear behavior to specimen height. The shear surface with taller asperities required a post-compression specimen height equivalent to 25 D_{50} to eliminate the boundary effects. Therefore, this specimen height was used in all the simulations. These dimensions enable specimens to contain about 127,000 particles.

INFLUENCE OF ASPERITY GEOMETRY ON SHEAR BEHAVIOR

The global behavior of the DEM interface shear simulations shows very similar trends to the experimental results observed in previous studies. Figure 3 shows the evolution of shear stress (τ) and average vertical displacement of the top plates (δ_V) as a function of horizontal displacement of the shear surface (δ_H). Simulations performed in the cranial direction (CR) are shown in blue, while simulations in the caudal direction (CD) are shown in brown. The behaviors of the rough and smooth surfaces plotted in black and grey behaved identically when sheared in either direction. As such, only one curve is presented for these surface geometries.

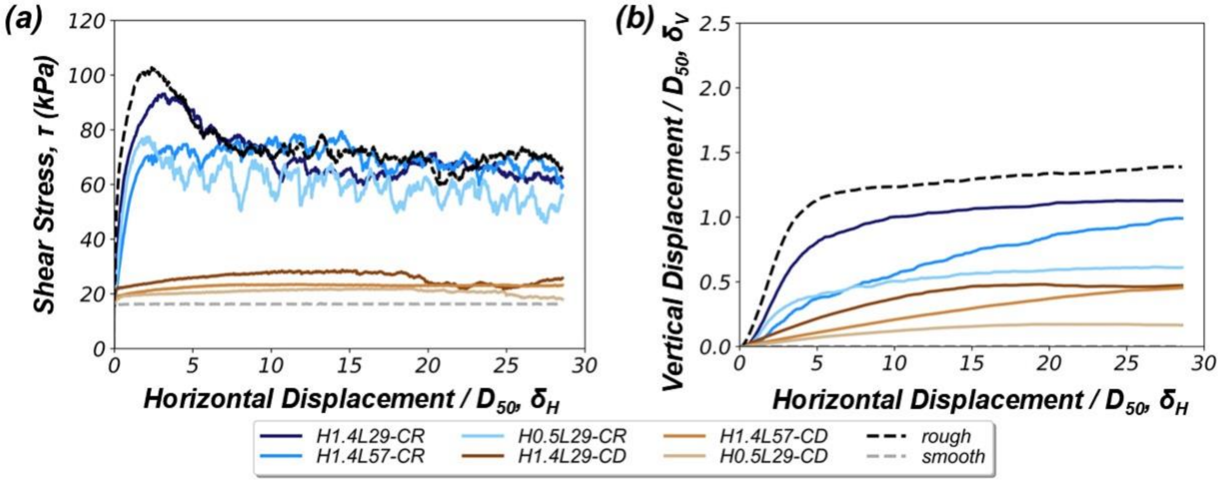

Figure 3. Shear stress (a) and average vertical displacement (b) as a function of horizontal displacement shear for smooth, rough, and snakeskin-inspired surfaces.

The mobilized shear strength increases with increasing H, decreasing L, and is significantly greater for cranially sheared specimens than caudally sheared ones. The cranially sheared snakeskin-inspired surfaces mobilize roughly the same residual strengths (τ_R) as the reference rough surface. The H1.4L29-CR surface, with the smallest L/H ratio, mobilizes the greatest peak shear strength (τ_P) among the snakeskin-inspired surfaces and exhibits strong strain softening in a similar manner to the rough surface. The other two snakeskin surfaces exhibit smaller strain softening magnitudes. The H0.5L29-CR surface mobilizes a similar τ_P as the H1.4L57-CR surface, while the τ_R for this surface is slightly lower. The differences in shear behavior due to asperity geometry are less pronounced in the caudal direction. The H1.4L29-CD surface mobilizes the greatest shear resistance followed by the H1.4L57-CD and H0.5L29-CD surfaces. The interface shear resistances mobilized in the caudal direction are slightly greater than those mobilized by the reference smooth surface. All three snakeskin-inspired surfaces have greater dilative tendencies when sheared cranially than caudally. Both snakeskin surfaces with L29 quickly reach their maximum dilations, while the L57 snakeskin surface dilates steadily through the test in both cranial and caudal directions. Surfaces with the lowest L/H ratio dilate the most, and dilation decreases as L/H increases.

PARTICLE LEVEL INTERACTIONS DURING INTERFACE SHEAR

The responses shown previously in Figure 3 arise from particle-level interactions that can be observed in DEM. During each simulation, particle displacements, rotations, and contact forces were tracked to analyze the particle interactions induced by the different surfaces and shear directions. The behaviors observed in this section provide insight regarding how asperity geometry affects shear behavior at both particle- and asperity-level.

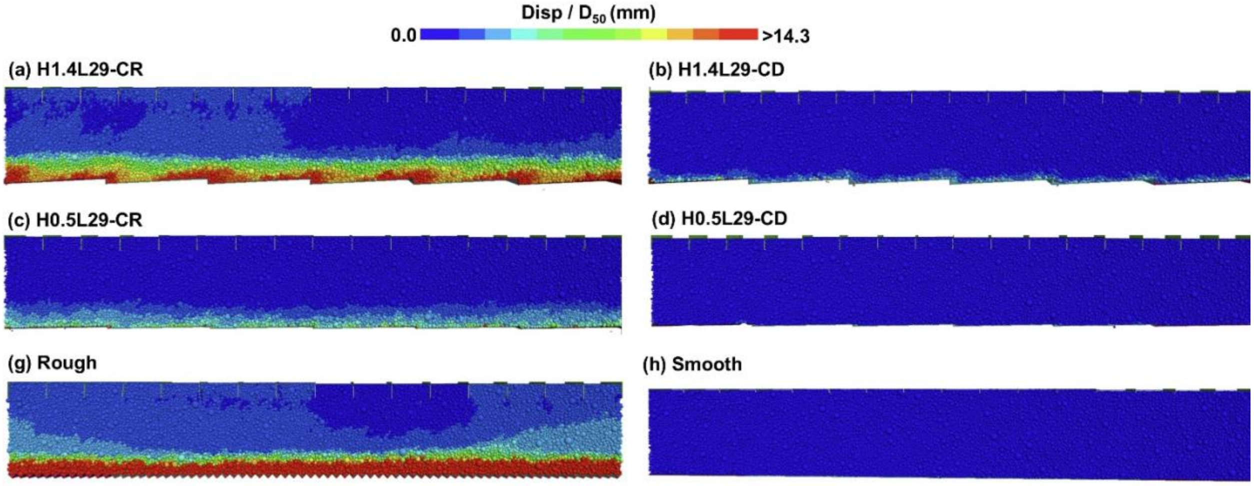

Figure 4. Total particle displacements at the end of shearing for smooth, rough, and snakeskin-inspired surfaces of select asperity geometries.

The total particle displacements at the end of the shearing stage for various surfaces are shown in Figure 4, where each particle is colored according to its total displacement magnitude. For the snakeskin-inspired surfaces, the particle displacement heavily depends on both geometry and shearing direction. The H1.4L29-CR simulation shown in Figure 4a has a clear, localized shear band near the bottom surface. Greater amounts of particle displacement occur around the corners of individual asperities. As particles encounter the edges of advancing asperities, they rearrange significantly. Particles are pushed upwards over the corners of asperities, where they then interact with the smooth frontal side of the asperity. When the shearing direction is reversed for H1.4L29-CD (Figure 4b), the particles slide over the smooth, frontal sides of the asperities. Only a small group of particles directly above the surface displaces while the rest of the soil mass remains stationary. These are shown at a lesser degree when H is reduced to 0.5 D_{50}. For H0.5L29-CR (Figure 4c), a localized shear band is still present. However, particles experience a smaller displacement in comparison to the H1.4L29-CR test. Particles still slide over the smooth, frontal sides of the asperities, though because less rearrangements occur, the shear resistance is smaller. Barely any particle displacements are observed for either H0.5L29-CD (Figure 4d) or for the smooth reference surface (Figure 4f). In either case, particles simply slide over the interface as it moves. Shearing against the rough surface (Figure 4e) produces a uniform shear band, dividing the specimen into a mobile zone near the soil-surface interface and an immobile zone at the top. Smaller particles are trapped in the areas between the sawteeth and move together with the surface.

The particle displacement fields suggest the formation of uniform shear bands during cranial shear (Figure 4). However, a better understanding of the failure mode can be obtained by analyzing the evolution of accumulated particle rotations over the course of shearing. This is done for H1.4L29-CR as shown in Figure 5. As shearing begins (Figure 5a), individual failure surfaces begin to form in front of each asperity. The arches of these surfaces encompass passive failure wedges where shear strains are localized. As shearing continues (Figure 5b), the failure surfaces become longer and flatter. Regions of particles that have undergone high rotations are observed around the corners of asperities. These particles were pushed upwards and over the asperities. The failure surfaces begin merging into one another to create a more uniform shear zone as the surface displacement is increased (Figure 5c). There remain pockets of particles ahead of advancing asperities that have undergone little rotations which are bound by the individual failure surfaces. The individual failure zones continue to merge together as shearing increases (Figure 5d and Figure 5e), while the pocket of particles with small rotations reduces in size. At the end of shearing, all localizations are contained in a well-defined shear band, as was observed in Figure 4a.

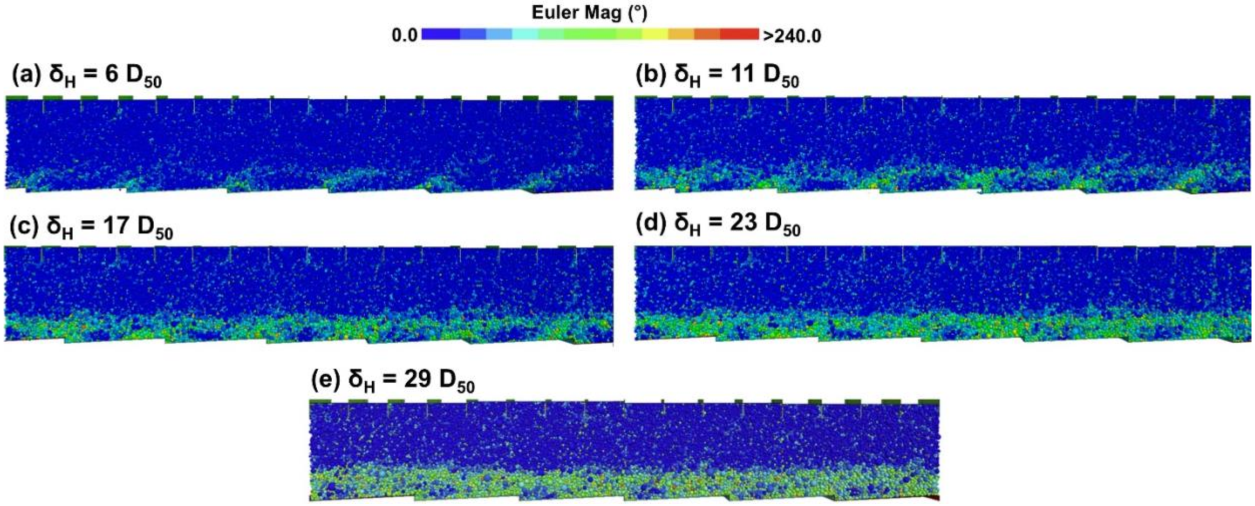

Figure 5. Particle rotations at various stages of shearing for asperities of H1.4L29-CR.

A closer look at the force chains mobilized within the specimen at the end of shearing shows distinct differences between the cranially and caudally sheared surfaces. Force chains are shown in Figure 6 for select asperity geometries. For the snakeskin inspired surfaces during cranial shear, strong contact forces are concentrated on the edges of the advancing asperities. These forces branch out into the rest of the soil mass in a diagonal direction. The surface with an H of 1.4 D_{50} (Figure 6a) mobilizes a greater number of strong force chains at each individual asperity compared to the surface of asperities with an H of 0.5 D_{50} (Figure 6c) due to the greater bearing area of the former. Additionally, the number of asperities present in the specimen plays a role in the mobilization of shear strength. For Figure 6a, L is 57 D_{50}, resulting in three asperities. As such, there are three zones in which strong force chains develop and form branch-like structures within the specimen. Figure 6c features a smaller L of 29 D_{50}, resulting in six asperities and thus double the number of force chain branches. This illustrates that the mobilized strength during cranial shearing is controlled by the height and number of asperities, with the latter being determined by the asperity length.

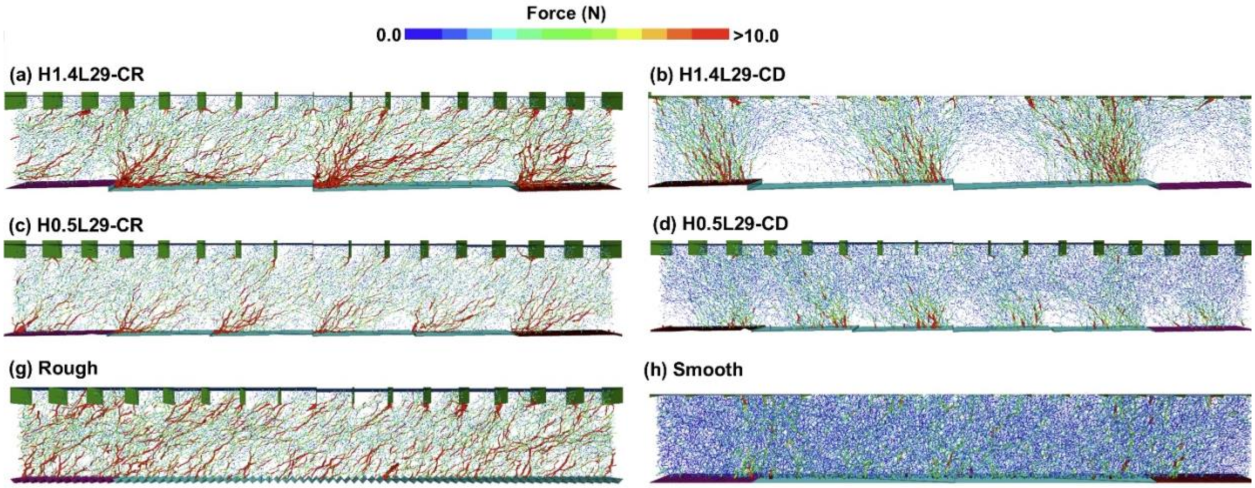

Figure 6. Force chains at the end of shearing for smooth, rough, and snakeskin-inspired surfaces of select asperity geometries.

For the caudally sheared surfaces, the force chains are concentrated on the front sides of the asperities, as shown in Figure 6b and Figure 6d. This is caused by the asperity's surface not being orthogonal to the direction of applied normal stress, resulting in a bearing load transfer component. H and L still play similar roles in caudal shear as they did in cranial shear. Namely, L controls the number of scales present in the specimen and as such controls the number of force chain branches. H and L affect the slope of the asperities, with greater heights and smaller lengths leading to greater slopes which mobilize stronger force chains.

The rough and smooth surfaces mobilized force chains that share similarities to those mobilized during cranial and caudal shear of snakeskin-inspired surfaces. The rough surface (Figure 6e) results in the mobilization of diagonal force chains scattered throughout the shear box. In contrast to cranial shearing with snakeskin-inspired surfaces, chains are not concentrated at specific locations, but rather span the full length of the shear box. The smooth surface (Figure 6f) produces primarily vertical force chains; however, some of the force chains with greater magnitudes lean towards the shearing direction.

CONCLUSIONS

This study investigated the load transfer mechanisms at the interfaces between snakeskin- inspired surfaces and sands through interface shear simulations using DEM. Five different shear surfaces were tested, including three snakeskin inspired surfaces with varying asperity height and length and reference rough and smooth surfaces. The interface shear strength mobilized by the snakeskin-inspired surfaces were strongly influenced by both asperity geometry and shear direction. As H increases and L decreases, the peak and residual strengths increase in both cranial and caudal shearing directions, in agreement with experimental investigations. Cranial shear mobilized significantly higher strengths than caudal shear. During cranial shear, individual passive failure zones merged together after sufficient shear displacement, creating more uniform shear zones. The asperity geometry had less of an impact for caudal shear, where less particle displacements occurred overall. Instead, particles primarily slid across the smooth sides of the asperities. In both directions, the number of asperities increases as L decreases, increasing the strength.

The results presented herein support previous studies in providing evidence for the potential benefits of geotechnical elements designed with snakeskin-inspired structures. This investigation also builds the foundation for a more in-depth DEM investigation of snakeskin inspired soil-structure interfaces. Future studies will investigate the influence of a greater variety of asperity geometries to better examine the role of H and L, different particle sizes, and a wider range of normal stress magnitudes. With a greater understanding of the micro mechanical processes influencing the overall behavior, the investigations performed in DEM will continue to shed light into the interactions of snakeskin-inspired soil-structure interfaces. Such investigations will also help in the development of design procedures for snakeskin-inspired surfaces for site-specific conditions.

REFERENCES

Blair, B. “Monotonic and Cyclic Resistance of MICP Cemented Silica and Carbonate Sands.” M.S. Thesis, *University of California Davis.* (2024).

DeJong, Jason T., and Zachary J. Westgate. “Role of Initial State, Material Properties, and Confinement Condition on Local and Global Soil-Structure Interface Behavior.” *Journal of Geotechnical and Geoenvironmental Engineering* 135, no. 11 (2009): 1646–60. https://doi.org/10.1061/(ASCE)1090-0241(2009)135:11(1646).

Frost, J. David, and Jason T. DeJong. “In Situ Assessment of Role of Surface Roughness on Interface Response.” *Journal of Geotechnical and Geoenvironmental Engineering* 131, no. 4 (2005): 498–511. https://doi.org/10.1061/(ASCE)1090-0241(2005)131:4(498).

Gayathri, V. L., Vangla, P., & Riya, A. (2022). Effect of snakeskin-inspired patterns on the shear response of soil - continuum interfaces. *International Journal of Geotechnical Engineering*, *16*(6), 759–775. https://doi.org/10.1080/19386362.2022.2066049.

Hryciw, Roman D., and Masyhur Irsyam. “Behavior of Sand Particles Around Rigid Ribbed Inclusions During Shear.” *Soils and Foundations* 33, no. 3 (1993): 1–13. https://doi.org/10.3208/sandf1972.33.3_1.

Jing, Xue-Ying, Wan-Huan Zhou, Hua-Xiang Zhu, Zhen-Yu Yin, and Yangmin Li. “Analysis of Soil-Structural Interface Behavior Using Three-Dimensional DEM Simulations.” *International Journal for Numerical and Analytical Methods in Geomechanics* 42, no. 2 (2018): 339–57. https://doi.org/10.1002/nag.2745.

Jensen, Richard P., Peter J. Bosscher, Michael E. Plesha, and Tuncer B. Edil. “DEM Simulation of Granular Media—Structure Interface: Effects of Surface Roughness and Particle Shape.” International Journal for Numerical and Analytical Methods in Geomechanics 23, no. 6 (1999): 531–47. https://doi.org/10.1002/(SICI)1096-9853(199905)23:6<531::AID-NAG980>3.0.CO;2-V.

Lee, Seung-Hun, Muhammad Naqeeb Nawaz, and Song-Hun Chong. “Estimation of Interface Frictional Anisotropy between Sand and Snakeskin-Inspired Surfaces.” *Scientific Reports* 13, no. 1 (March 9, 2023): 3975. https://doi.org/10.1038/s41598-023-31047-3.

Lings, M. L., and M. S. Dietz. “The Peak Strength of Sand-Steel Interfaces and the Role of Dilation.” *Soils and Foundations* 45, no. 6 (2005): 1–14. https://doi.org/10.3208/sandf.45.1.

Martinez, Alejandro. “Skin Friction Directionality in Monotonically- and Cyclically-Loaded Bio-Inspired Piles in Sand.” *DFI Journal The Journal of the Deep Foundations Institute* 15 (April 2021). https://doi.org/10.37308/DFIJnl.20200831.222.

Martinez, Alejandro, and J. Frost. “The Influence of Surface Roughness Form on the Strength of Sand–Structure Interfaces.” *Géotechnique Letters* 7 (March 2017): 1–8. https://doi.org/10.1680/jgele.16.00169.

Martinez, Alejandro, Sophia Palumbo, and Brian D. Todd. “Bioinspiration for Anisotropic Load Transfer at Soil–Structure Interfaces.” *Journal of Geotechnical and Geoenvironmental Engineering* 145, no. 10 (2019): 04019074. https://doi.org/10.1061/(ASCE)GT.1943-5606.0002138.

O’Hara, Kyle B., and Alejandro Martinez. “Monotonic and Cyclic Frictional Resistance Directionality in Snakeskin-Inspired Surfaces and Piles.” *Journal of Geotechnical and Geoenvironmental Engineering* 146, no. 11 (2020): 04020116. https://doi.org/10.1061/(ASCE)GT.1943-5606.0002368.

K.B. O'Hara and A. Martinez. "Cyclic axial response and stability of snakeskin-inspired piles in sand." Acta Geotechnica, 19, no. 3 (2024). 10.1007/s11440-023-02007-y

Uesugi, Morimichi, and Hideaki Kishida. “Frictional Resistance at Yield between Dry Sand and Mild Steel.” *Soils and Foundations* 26, no. 4 (1986): 139–49. https://doi.org/10.3208/sandf1972.26.4_139.

Xiao, Yang, Hao Cui, Jinquan Shi, Wenhao Qiao, and Armin W. Stuedlein. “Shear Response of Calcareous Sand-Steel Snake Skin-Inspired Interfaces.” *Acta Geotechnica* 19, no. 3 (March 1, 2024): 1517–27. https://doi.org/10.1007/s11440-023-02151-5.

Zhong, Wenhan, Hanlong Liu, Qi Wang, Wengang Zhang, Li Yongqin, Xuanming Ding, and Longlong Chen. “Investigation of the Penetration Characteristics of Snake Skin-Inspired Pile Using DEM.” *Acta Geotechnica* 16 (June 2021): 1–17. https://doi.org/10.1007/s11440-020-01132-2.

The paper was published in the proceedings of the 2025 International Conference on Bio-mediated and Bio-inspired Geotechnics (ICBBG) and was edited by Julian Tao. The conference was held from May 18th to May 20th 2025 in Tempe, Arizona.